Comput Geosci (2007) 11:297–306
DOI 10.1007/s10596-007-9053-y

ORIGINAL PAPER

SPH-based numerical investigation of mudflow and other complex fluid flow interactions with structures

Dominique Laigle · Philippe Lachamp · Mohamed Naaim

Received: 6 September 2006 / Accepted: 10 May 2007 / Published online: 31 July 2007

Abstract The understanding of mudflow–structure interactions and debris–flow structure interactions is of paramount importance for the rational design of technical countermeasures. However, to date, only a limited number of studies have investigated this subject. We propose here a numerical approach to this topic using a 2D vertical numerical model based on the smoothed particle hydrodynamics (SPH) method. First, we will test the capacity of the model to simulate unsteady free-surface flows of water and viscoplastic fluid in comparison to laboratory experiments. Then, we will use it prospectively, based on a series of simulations of Bingham fluid free-surface propagations, to determine the momentum reduction resulting from the presence of a simple obstacle perpendicular to the direction of propagation and to determine the characteristics of stresses applied to this obstacle in terms of peak pressure and evolution over time.

Keywords Mudflow · Debris flow · Simulation model · Dynamic impact · Protection structures

1 Introduction

Mudflows and debris flows are rapid gravity-driven unsteady flows of highly concentrated mixtures of water and solid material with large grain size distribution. These flows can cause major damage to human infrastructures, especially damage resulting from the impact force potentially exerted by the flow front. Many structures protecting against mudflows and debris flows are installed in torrent channels [8], and for the most part, are submitted to normal impacts. These technical protection structures are set up to reduce the flow dynamics and the subsequent destructive effects. In addition, they have to be designed to resist the force of the impact generated by the flow. However, to date, the interaction between mud or debris flows and these structures has rarely been studied in detail [1, 26]; as a result, these structures are still designed mainly on the basis of empirical rules. In this context, the first goal of the study reported herein was to characterize the influence of protection structures on mudflows and debris flows, mainly to quantify the momentum reduction caused by the structure. It is also necessary to characterize the force of the impact applied on the structure. The resistance of structures submitted to dynamic impacts depends upon the peak intensity of applied stresses, their spatial distribution, but also their evolution over time, which must be compared with the structure's specific reaction time. The second goal of the present work was to study flow characteristics in the vicinity of the structure to deduce features of the stresses applied to it by mudflow or debris-flow impacts. This study can also help in estimating potential damage to buildings or other human infrastructures.

Most of the existing models simulating mudflow and debris-flow propagation (see [24], for examples) are based upon the depth-averaged approach [9]. The most sophisticated of these models have proved their ability to accurately simulate flows of fluidized granular masses [5] or dry granular avalanches [6, 10, 21] across complex three-dimensional terrain, showing that the influence of many

---

D. Laigle (✉) · M. Naaim
Cemagref, Snow Avalanche and Torrent Control Research Unit,
BP 76, F-38402 Saint-Martin-D'Hères Cedex, France
e-mail: dominique.laigle@cemagref.fr

P. Lachamp
BULL S.A, HPC Linux, 1, rue de Provence,
Echirolles, F-38130, France

types of structures on the flow can be captured by these models. Furthermore, the interaction of granular free-surface flows with obstacles was investigated in detail by Gray et al. [7], who proved, by comparison with laboratory experiments, that the depth-integrated approach can accurately simulate the features of the flow in the vicinity of a three-dimensional obstacle, and in particular, it can simulate complex processes such as the formation of shock waves, dead zones, or particle-free regions. However, the depth-integrated approach suffers from a major limitation: only depth-integrated values of velocities or pressures, for instance, are computed, and all information on local values along the vertical direction is lost. As a consequence, the distribution of stresses applied to the upstream face of a structure submitted to a normal impact cannot be studied in detail when using this type of model. For this reason, a modeling approach taking the vertical direction explicitly into account has been preferred.

The theoretical study of the flow–structure interaction that we present in this paper is based on the 2D vertical model developed by Lachamp [14]. This model stems from the smoothed particle hydrodynamics (SPH) numerical method. SPH is a particle method for treating fluid mechanics equations, typically Navier–Stokes equations [20]: particles used in the method are not physical, they must be considered as a means of representation of a fluid having rheological characteristics given by an apparent viscosity. This apparent viscosity makes it possible to handle different types of fluids. In the present study, we considered viscoplastic fluids with a Bingham or Herschel–Bulkley type of rheological behavior suitable for mudflows or viscous debris flows [4, 11, 23]. But other types of rheology, suitable for granular flows, for example, have been successfully tested, as reported by Lachamp et al. [13], who use an approach similar to that proposed by Jop et al. [12], or as reported by Rodriguez-Paz and Bonet [25]. After specific treatment of the fluid–channel bed interaction [19], SPH is suitable for computing highly transitory free-surface flows of complex fluids in complex geometries. The present model presents similarities with the one proposed by Rodriguez-Paz and Bonet [25]. These authors use a slightly different cut-off function and equation of state (see below) and also consider the generalized viscoplastic fluid model proposed by Chen [2]. As pointed out by Rodriguez-Paz and Bonet [25], several other numerical methods could have been used to simulate mud or debris-flow–structure interactions, especially the particle in cell method, the finite difference, finite volume or finite element methods. Using a computation mesh structure, these methods all present the time-consuming problem of remeshing the flow domain as the solution advances in time. In addition, other mesh-free methods, such as the discrete element method, adopt a noncontinuum approach that does not allow a fluid constitutive equation to be introduced. In that context, SPH can be seen as an alternative to other more classical methods, presenting the advantage of solving the fluid mechanics equations with relative simplicity, without the problem of mesh structure and the ability to compute free surfaces and flows easily across complex geometries.

This paper first presents the main features of the SPH model with specific attention given to the treatment of boundary conditions and rheological behavior. SPH simulations of unsteady free-surface flows of water and viscoplastic fluids are compared to experimental flows, with no obstacle, of water and kaolin clay–water mixtures, respectively. Then we present a series of numerical simulations of Bingham fluid transitory flow–obstacle interactions. The influence of the obstacle on both flow depth and momentum is analyzed. Results are systematically compared to reference flows (the same conditions but with no obstacles). The evolution of local dynamic pressures applied to the obstacle over time is also simulated. Values of the peak intensity of pressures applied to the structure are given and compared to those of the reference flow. Finally, the evolution of the pressures over time is analyzed.

2 The SPH method

2.1 Presentation

SPH is a particle Lagrangian method that solves the classical equations of fluid dynamics. It was originally developed to simulate astrophysical phenomena [16, 18]. A great deal of research has been conducted on compressible fluids, but there are fewer studies on incompressible fluids in the literature. To simulate incompressible fluid flows, the most common technique consists in considering them as weakly compressible fluids [20]. The momentum equation for incompressible fluids [Eq. (1)] is thus solved; in the meantime, the continuity equation for compressible fluids [Eq. (2)] is solved. This method is the most frequently used, even when compressible fluid flows are considered [17, 18]. The SPH method is able to compute the position of the free surface of gravity-driven flows without specific treatment (Fig. 1). The model computes local values of pressure and velocity, two essential variables in the study of flow–structure interactions. Pressure is computed using a state equation, taking into account both hydrostatic and dynamic effects. The model presented here is two-dimensional in the vertical direction, and extension to a full 3D model presents no theoretical problem. Only the treatment of boundary conditions is slightly more difficult. However, for reasons of computation time, we preferred to refrain from using 3D analysis.

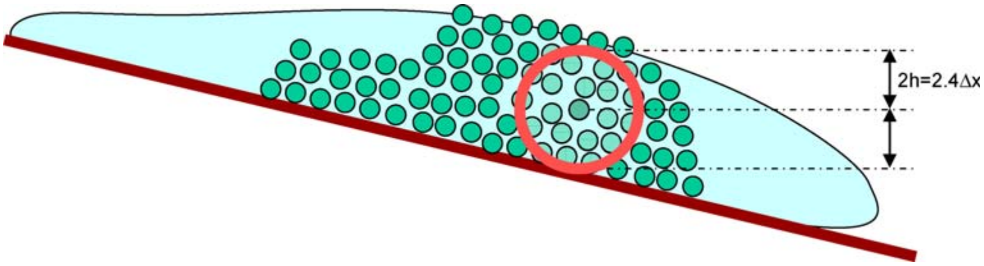

Fig. 1 Schematic view of SPH particles constituting the fluid domain submitted to a gravity-driven flow. *Inside the circle*: particles that have an influence on the central particle

2.2 SPH equations

2.2.1 Classical formalism

Equations of motion are based upon the classical continuity and momentum equations for fluids interpolated between unphysical particles, which have to be considered as a discrete representation of a continuum. The interpolation is based on a classical quadrature technique using a cut-off function whose limit is a Dirac around the particle considered. The most common cut-off function [19] is written:

$$W(s) = \frac{C}{h^{\lambda}} \begin{cases} 1 - \frac{3s^2}{2} + \frac{3s^3}{4}, & 0 \leq s \leq 1 \\ \frac{1}{4}(2-s)^3, & 1 \leq s \leq 2 \\ 0, & s \geq 2 \end{cases} \tag{1}$$

where $s = \frac{|r|}{h}$ $\left(r = \left\| \vec{r} \right\|\right.$ is the distance between two particles, and h depends on the initial spatial step Δx: for the 2D case, $h \cong 1.2\Delta x$), λ is the dimension of space, and C takes the values $\frac{2}{3}, \frac{10}{7\pi}, \frac{1}{\pi}$, respectively, for $\lambda=1$, 2, and 3. This polynomial form provides a strictly compact support to the cut-off function W (Fig. 2).

Let us consider the classical momentum equation of incompressible fluid mechanics:

$$\frac{d\vec{u}}{dt} = \nabla.\left(\frac{1}{\rho}\underline{\underline{\sigma}}\right) + \vec{F} \tag{2}$$

and the continuity equation of compressible fluid mechanics:

$$\frac{\partial \rho}{\partial t} = \nabla.(\rho \vec{u}) \tag{3}$$

For free-surface flows, the source term $\vec{F}$ reduces to gravity $\vec{g}$. $\vec{u}$ is the velocity vector, and $\underline{\underline{\sigma}}$ is the full Cauchy tensor.

Using SPH formalism, the momentum equation is expressed as:

$$\frac{du_{\alpha}^{i}}{dt} = \sum_{\beta \in G} m_{\beta} \left(\frac{\sigma_{ii}^{\alpha} + \sigma_{ii}^{\beta}}{\rho_{\alpha}\rho_{\beta}} + \Pi_{\alpha\beta} \right) \frac{\partial W_{\alpha\beta}}{\partial x_i} + \sum_{\beta \in G} m_{\beta} \left(\frac{\sigma_{ij}^{\alpha} + \sigma_{ij}^{\beta}}{\rho_{\alpha}\rho_{\beta}} \right) \frac{\partial W_{\alpha\beta}}{\partial x_j} + g_i \tag{4}$$

and the continuity equation is expressed as:

$$\frac{\partial \rho_{\alpha}}{\partial t} = \sum_{\beta \in G} m_{\beta} \vec{u}_{\alpha\beta}.\vec{\nabla}_{\alpha} W_{\alpha\beta} \tag{5}$$

where exponents i and j stand for any coordinate with $i \neq j$. Each particle α (resp. β) has a mass m_{α} (resp. m_{β}), a velocity vector given by its coordinates u_{α}^{i} (resp. u_{β}^{i}, with $\vec{u}_{\alpha\beta} = \vec{u}_{\alpha} - \vec{u}_{\beta}$), a stress tensor $\underline{\underline{\sigma}}(\alpha)$ (resp. $\underline{\underline{\sigma}}(\beta)$), and a density ρ_{α} (resp. ρ_{β}). G is the set of particles in the domain of interest. The derivative of W versus coordinates of particle α is written as:

$$\frac{\partial W_{\alpha\beta}}{\partial x_i} = \frac{\partial}{\partial x_i} W\left(\frac{r_{\alpha\beta}}{h}\right) \tag{6}$$

where $r_{\alpha\beta} = \left\| \vec{r}_{\alpha\beta} \right\|$ is the distance between particles α and β. After Monaghan and Gingold [17], $\Pi_{\alpha\beta}$ is a numerical viscous pressure possibly used when, for example, shocks are considered:

$$\Pi_{\alpha\beta} = \begin{cases} \frac{-ac\mu_{\alpha\beta} + b\mu_{\alpha\beta}^{2}}{\rho_{\alpha\beta}^{*}}, & \vec{u}_{\alpha\beta} \cdot \vec{r}_{\alpha\beta} < 0 \\ 0, & \vec{u}_{\alpha\beta} \cdot \vec{r}_{\alpha\beta} \geq 0 \end{cases} \tag{7}$$

with:

$$\mu_{\alpha\beta} = \frac{h\vec{u}_{\alpha\beta} \cdot \vec{r}_{\alpha\beta}}{r_{\alpha\beta}^{2} + \eta^{2}} \tag{8}$$

and the average value of the density of particles α and β:

$$\rho_{\alpha\beta}^{*} = \frac{m_{\alpha}\rho_{\alpha} + m_{\beta}\rho_{\beta}}{m_{\alpha} + m_{\beta}} \tag{9}$$

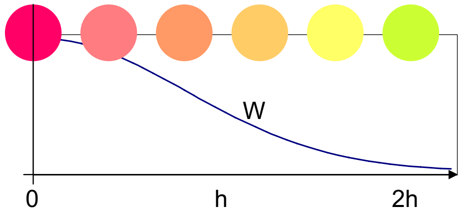

Fig. 2 Cut-off function *W*, illustration of the intensity of the interaction of the central particle (*left*) with its neighbors versus their respective distance

For the treatment of free-surface flows, we adopt a= 0.01, b=0, and η=0.1 h [20]. c is the "average speed of sound" of particles α and β.

2.2.2 Equation of state

As pointed out by Monaghan [20], one possible technique to simulate incompressible flows with SPH would be to work directly with the constraint of constant density. However, considering that real fluids, such as water, are compressible is generally preferred, with the assumption that their speed of sound is much greater than the speed of bulk flow. In fact, compressibility and speeds of sound and bulk flow are linked by $\frac{\Delta\rho}{\rho} = M^2$ (M is the Mach number and is defined as $M = \frac{\left\|\vec{u}\right\|}{c}$). Thus, when the speed of sound (~10^3 m s^{-1} for water) is ten times the maximum bulk flow velocity, the maximum compressibility is 1%.

SPH requires computing the pressure of each particle. To achieve this, an equation of state is used that computes the pressure value on the basis of density. We have adopted the following simple expression, which gave satisfactory results [12]:

$$P_\alpha = P_0 + c^2(\rho_\alpha - \rho_0) \tag{10}$$

where P_α and ρ_α are the pressure and density of particle α, P_0 and ρ_0 are constants generally taken as equal to the initial pressure and density, respectively. First, it can be noted that the relation $\frac{\partial P_\alpha}{\partial \rho_\alpha} = c^2$ is verified. We can then define the dynamic pressure as $P_\alpha = \rho_\alpha \left\|\vec{u}_\alpha\right\|^2$ and note that it does not depend on the speed of sound, so that we are allowed to choose a low, nonphysical value of c to increase the time step in the application of SPH, provided the adopted speed of sound value is sufficiently higher (at least 10 times, according to Rodriguez-Paz and Bonet [25]) than the maximum speed of the bulk flow considered. In fact, this technique has limited influence on computed velocities, but greatly affects computed densities and therefore pressures. Without further treatment, the pressure of each particle varies rapidly around a mean value. To obtain a realistic pressure distribution, it was necessary to adopt a smoothing technique. This technique consists in regularly imposing (every n time steps), to each particle, a density value equal to the mean value over these n time steps of densities associated with this particle. A typical value of approximately 20 for this parameter n gave precise representations of the hydrostatic distribution of pressures inside a steady flow and realistic pressure distributions inside a highly transitory flow. As a consequence, one can deduce that the physical significance of local and instantaneous values of some of the flow variables and particularly the pressures, can be uncertain. We will come back to this problem in the Section 4.

2.2.3 Introduction of fluid behavior in the SPH method

Here, we consider mudflows and viscous debris flows to be Herschel–Bulkley fluid flows [4, 23]. Within the SPH approach, this rheology can be implemented using local apparent viscosity whose value depends on the local shear rate. To explain the procedure adopted, we first express the Cauchy tensor used in equation (4), which can be written as:

$$\underline{\underline{\sigma}} = -P\delta_{ij} + \underline{\underline{T}} \tag{11}$$

where P is the pressure, δ_{ij} is the Kroneker symbol, and $\underline{\underline{T}}$ is the deviatoric extra-stress tensor. The constitutive equations for the rigid-viscoplastic Herschel–Bulkley model (and its reduction to Bingham's model) are [22]:

$$\begin{aligned} \underline{\underline{T}} = 2\mu\underline{\underline{D}} \quad \text{if} \quad \sqrt{\frac{tr\underline{\underline{T}}^2}{2}} > \tau_c \\ \underline{\underline{D}} = 0 \quad \text{if} \quad \sqrt{\frac{tr\underline{\underline{T}}^2}{2}} \leq \tau_c \end{aligned} \tag{12}$$

where $\underline{\underline{D}}$ is the rate of deformation tensor and μ is the apparent local dynamic viscosity given by:

$$\mu = K\sqrt{2tr\underline{\underline{D}}^2}^{(n-1)} + \frac{\tau_c}{\sqrt{2tr\underline{\underline{D}}^2}} \tag{13}$$

which combines the yield stress τ_c, the power-law index n, and the liquid consistency K. In the special case of n=1, the Herschel–Bulkley model reduces to the Bingham model. Numerically, it is necessary to adopt a maximum value $\mu_{\max}$ of the viscosity when the shear rate $\dot{\gamma} = \sqrt{2tr\underline{\underline{D}}^2}$ becomes very small. An example of the evolution of apparent viscosity versus shear rate is given in Fig. 3. It should be noted that this concept of apparent local viscosity can be used to simulate a large number of fluids. One can consider that the viscosity depends upon the local shear rate, as is done here, but also for example on normal stresses, as would be required to simulate

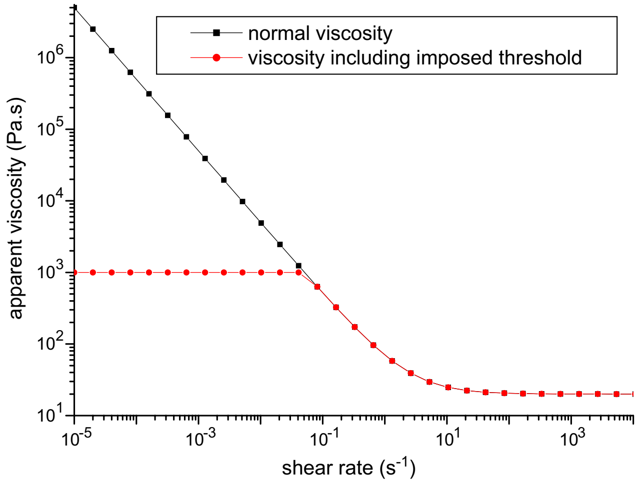

Fig. 3 Example of the evolution of local viscosity versus the shear rate for a Bingham fluid with $\mu_{\text{app}} = \min\left(\frac{50.}{\dot{\gamma}} + 20., 1000.\right)$

granular flows. In addition, it is possible to simulate several fluids showing different features inside the same computation domain, as has been done by Lachamp [14].

2.2.4 Boundary conditions

Let us consider here the influence of walls limiting the flow domain. First, it is necessary to ensure that fluid particles close to the wall are submitted to a repulsive force depending upon the distance to the wall [20]. For the viscous fluids considered here, it is also necessary to ensure a no-slip condition of the flow at the wall.

In our case, the treatment adopted for boundary conditions consists in building "ghost" particles, symmetrical to fluid particles with reference to the wall, whenever they are at a distance lower than $2h$ [see Eq. (1)] from the wall. To ensure a no-slip condition, the ghost particle velocity is opposite its symmetrical fluid particle (Fig. 4). Pressure and viscosity of ghost particles must also be defined. For example, when considering free-surface flows, adopting the same pressure and viscosity for fluid and ghost particles would lead to a breakpoint in the pressure and viscosity gradients when crossing the bottom wall. Extrapolating the pressure and viscosity beyond the wall and imposing subsequent values to ghost particles is then preferred (Fig. 5).

3 Comparison to experiments with no obstacles

The goal of this study was to compare SPH simulations to experimental unsteady flows of water or viscoplastic fluids of the dam-break type. Two sets of experimental data were used. The first set comes from Martin and Noyce (1952) reported by Monaghan [19]. It concerns water propagation in a horizontal flume. Available data are the surge front position and the height of the fluid column collapsing under gravity versus time. The second set comes from experiments we carried out in an inclined flume, using a viscoplastic fluid. In this latter case, the experimental equipment consists of a rectangular cross-section inclined flume, 5 m long and 0.3 m wide. The model fluid is a mixture of kaolin clay and water. This mixture is initially stored upstream of a sluice gate, which is instantaneously opened when the flow is triggered. The experimental procedure is similar to that presented in Laigle and Coussot [15]. Rheological properties of the mixture were measured independently using a rheometer and parameters of the Herschel–Bulkley constitutive law fitted to rheometrical data, assuming a power-law index $n=1/3$, as proposed by Coussot [3]. Four experiments were carried out in similar conditions. Data measured on the viscoplastic fluid flow, using a video camera, concern only the surge front position versus time.

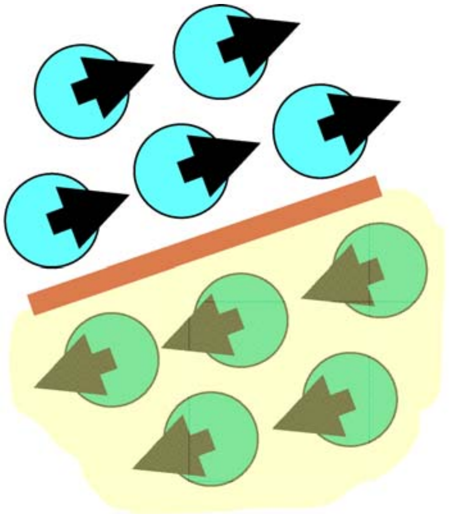

Fig. 4 Computation of boundary conditions with ghost particles located symmetrically to fluid particles with reference to the wall and opposite velocity vectors to represent the no-slip condition

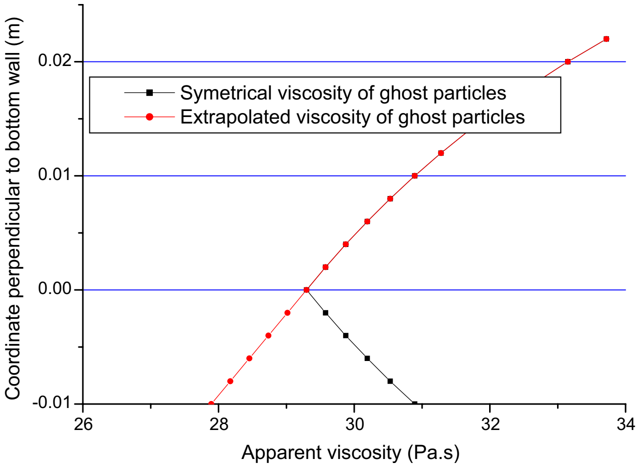

Fig. 5 Example of extrapolation of fluid particle viscosity to compute ghost particle viscosity. *Bottom wall* is located at coordinate $y=0$

Characteristic dimensions of both experiments are defined in Fig. 6, and results are plotted in Figs. 7 and 8, using dimensionless time and length of surge front propagation. SPH simulations of viscoplastic fluid propagation were

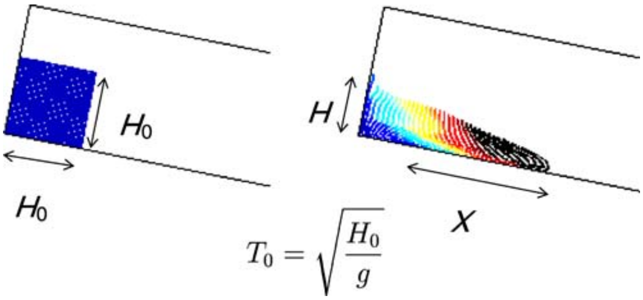

Fig. 6 Definition of variables used in the comparison to experimental propagation

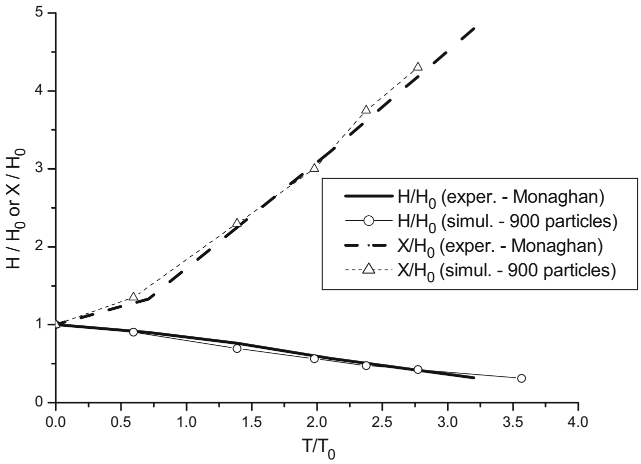

Fig. 7 Comparison of SPH simulations to the experiments of free surface water surge propagation reported in Monaghan [20]. *T* is time; other variables are defined in Fig. 6

carried out with 2500 particles and water propagation with 900 particles. Figures 7 and 8 show good agreement between simulated and experimental surge front propagation versus time for both fluids. Figure 7 shows excellent agreement between simulated and experimental evolution of the height of water column versus time. These results were obtained without calibration of any friction coefficient or rheological parameter. Monaghan's [20] computation of the surge front position does not match the experimental data as well as our own computation reported in Fig. 7. To explain the slight discrepancy observed, Monaghan speculates the effect of basal drag not accounted for in his SPH calculation. The main differences between Monaghan's model and our model bear upon the equation of state and the treatment of boundary conditions. But while Monaghan considered only a repulsive force depending upon the distance of fluid particles to the wall, we adopted techniques which also ensure a no-slip condition of the flow at the wall (see Section 2.2.4). One can reasonably assume that this no-slip condition is more appropriate and explains why our simulations better match experimental data.

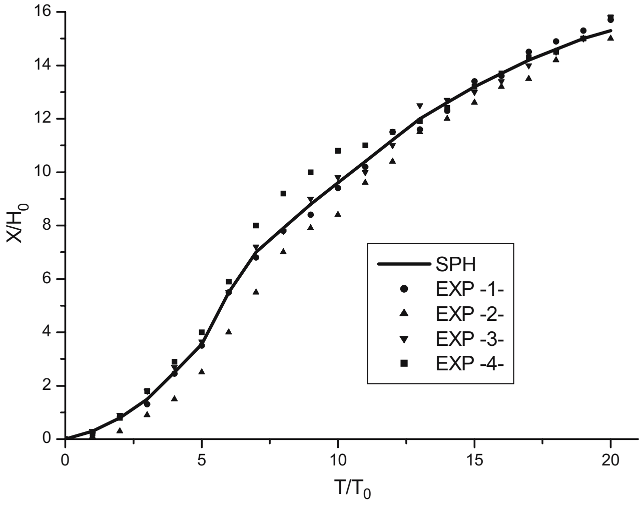

Fig. 8 Comparison of SPH simulation to a series experiments of mud propagation. *T* is time; other variables are defined in Fig. 6

Apart from the results presented in the present paper, Rodriguez-Paz and Bonet [25] also successfully simulated experimental and natural avalanches of dry granular material. Thus, one can consider that the capacity of SPH to simulate the propagation of surges of various types of fluids, including viscoplastic fluids, has been proved. This was a compulsory basis to the numerical investigation of the flow–structure interaction presented below.

4 Interaction of unsteady flows with obstacles

4.1 Presentation of simulations

This part numerically analyzes the effect of geometrically simple fixed and rigid obstacles on unsteady flows of yield stress fluids. Simulations are the result of dam-break-type propagations carried out in similar conditions with a limited volume of material and defined as follows.

Only one Bingham fluid is considered with apparent viscosity (in Pa s) given by: $\mu_{\text{app}} = \min\left(\frac{35.}{\dot{\gamma}} + 20.,1000.\right)$. The steepness of the inclined flume is either 10 or 20%. Initial depth of material H_0=0.3 m (Fig. 6). An obstacle consisting of a wall perpendicular to the flume bottom is located at abscissa $X_{\text{obs}} = \frac{10}{3} H_0 = 1.0$ m. The height of the obstacle H_{obs}=1, 2, 3, 4, or 5 cm. We also define three observation points or "sensors" downstream from the obstacle at abscissa $X_1 = 4.H_0 = 1.2$ m, $X_2 = 5.H_0 = 1.5$ m, and $X_3 = 6.H_0 = 1.8$ m (Fig. 9). Each of these sensors records the instantaneous velocity, discharge, momentum, and kinetic energy and the momentum and kinetic energy integrated over a period of time. Computations are limited to a maximum real flow time $T_{\max}$=10 s, which corresponds to a very slow flow, close to stoppage. The main goals of this prospective part are, on the one hand, to estimate the influence of the obstacle on the flow by comparison between flows with and without an obstacle (the latter called the reference flow) downstream of the obstacle position. On the other hand, we study the dynamic pressures applied to the obstacle and compare them to pressures developed inside the reference flow.

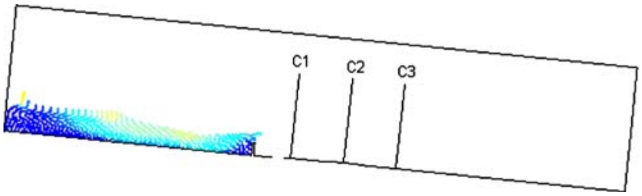

Fig. 9 Schematic positions of sensors in the flume

4.2 Momentum reduction due to structure

We define the instantaneous momentum as follows: as the flow is almost one-dimensional, only the component u of the velocity parallel to the bed is considered, and its product to density is integrated on flow depth h. Thus, the momentum is written as:

$$mom = \int_0^h \rho u(z).dz \tag{14}$$

In fact, numerically, it is computed in 2D by summing all $m_i u_i$ of particles i present in a band perpendicular to the bed whose width is given by Δx, the initial spatial step. Figure 10 gives an example of this type of result at sensor position X_1. It should be noted that we consider here local and instantaneous values of particle velocities. The time-scale of records is thus relatively small compared to the smoothing time scale presented in paragraph 2.2.2. This explains the rather noisy signal observed in Fig. 10. In fact, this observation of local and instantaneous flow variables takes place at a scale, which given the inevitably limited number of particles, is at the limit of SPH capacity to simulate real flows. Results obtained at this spatial and time scale have to be considered carefully. To reduce this problem and also to better estimate the influence of the obstacle by comparison to the reference flow, it is worth considering the momentum integrated on time and defined as:

$$imom(T) = \int_0^T mom(t).dt \tag{15}$$

Using this expression, the difference between flows with and without an obstacle is clearly shown, and when the flow stops, the difference of integrated momentum is actually the momentum absorbed by the obstacle. An example of the evolution of the integrated momentum over time is given in Fig. 11, which shows the general trend of a momentum reduction that clearly depends upon obstacle height (in the range $0 \leq H_{obs} \leq 5$ cm). An overview of the results obtained for various slopes and sensor positions is given in Table 1, which compares integrated momentum of flows with an obstacle to the reference flow at time T_{max}= 10 s. We first note that the relative influence of an obstacle with a given height is systematically lower at the steeper slope. For example, with an obstacle height H_{obs}=5 cm, integrated momentum reduction ranges from 56 to 86% on a 10% slope, whereas it ranges from 27 to 33% on a 20% slope. We also note that the reduction in integrated momentum increases with the distance between the obstacle and the sensor considered, so that at a similar slope, this reduction is systematically higher at sensor position X_3 than at X_1. As the results in Table 1 are established at a given time, it may be that a longer simulation time would reduce the difference between successive sensor positions. To check this, a few simulations with a much longer maximum time of 120 s were carried out, but we concluded that increasing the time does not substantially modify the results.

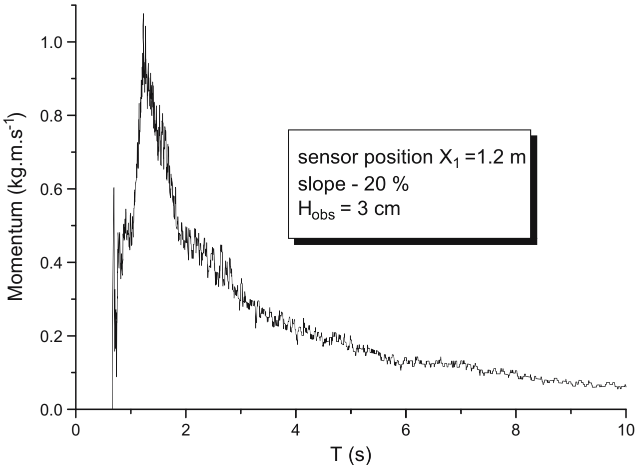

Fig. 10 Example of the evolution of flow momentum versus time

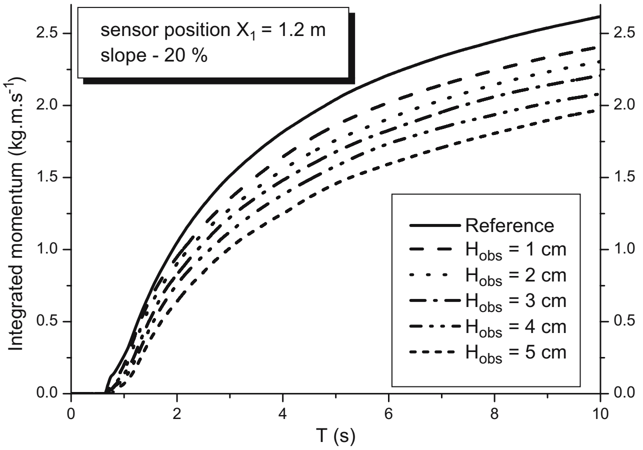

Fig. 11 Examples of the evolution of integrated momentum versus time

Table 1 Influence of obstacle height H_{obs} on the flow momentum downstream of the obstacle, comparison to the reference flow momentum

Slope	10%			20%		
Sensor	X_1	X_2	X_3	X_1	X_2	X_3
H_{obs}=1 cm	0.77	0.65	0.46	0.89	0.86	0.82
H_{obs}=2 cm	0.69	0.58	0.37	0.86	0.83	0.78
H_{obs}=3 cm	0.62	0.51	0.27	0.82	0.79	0.74
H_{obs}=4 cm	0.53	0.38	0.14	0.77	0.75	0.70
H_{obs}=5 cm	0.44	0.31	0.14	0.73	0.71	0.67

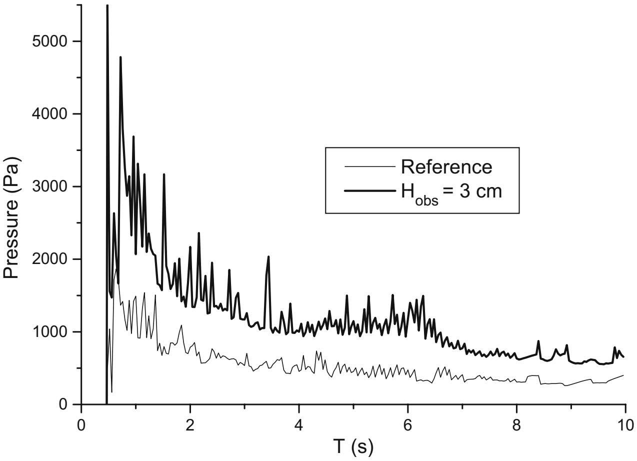

Fig. 12 Evolution of pressure versus time at slope=20%, comparison between the reference and obstacle flows with an obstacle height of 3 cm

The momentum reduction can originate in the flow depth reduction or in the flow velocity reduction. In fact, it was noted that the presence of an obstacle tends to reduce the flow depth at sensor positions in a range generally between 0 and 20%, while the reduction in integrated momentum can, for example, reach values as high as 86% at sensor position X_3 on a 10% slope and height of obstacle H_{obs}= 5 cm. Consequently, the presence of the obstacle essentially tends to reduce the flow velocity.

4.3 Stresses applied to the structure

Because of the unsteady nature of the flows considered, the pressure applied to structures is rather dynamic. In this sense, the design of protection structures should consider the evolution of pressure over time, especially its rising phase, as well as its maximum value. All results presented here consider the dynamic pressure in the vicinity of the upstream face of the obstacle.

4.3.1 Maximum pressure applied to the obstacle

Pressures are observed here within a rectangular "window" in contact with the upstream face of the obstacle, with the same height as this obstacle and a width equal to $2\Delta x$ (see Section 2.2.1). The pressure considered here is, at any time, the maximum pressure value of any particle inside this window. In that sense, it must be considered as a local pressure and not as a mean pressure applied to the upstream face of the structure. The evolution of the maximum pressure over time is given in Fig. 12 for an obstacle height of H_{obs}=5 cm and a 20% slope and compared to the pressure of the reference flow with no obstacle at the same location. In fact, the pressure of the reference flow is always very close to the simple hydrostatic pressure at the bottom wall and is closely related to the flow depth. Even for long simulation times, the pressure does not return to zero. When an obstacle is present, this is due to the mass of material trapped upstream of the structure, and when there is no obstacle, it is attributable simply to the effect of the yield stress governing the thickness of deposits.

In Fig. 12, both obstacle and reference flows show a pressure peak shortly after the first contact between the flow and the obstacle. The latter shows a very rapid rise in the pressure with a high peak value. This peak is followed by a very rapid drop and a secondary peak. This secondary peak, however, was not systematically observed in all simulations. After the peak, both flows show a rapid decrease in pressure, which then gradually becomes slower and slower, reaching a quasi-constant pressure value after a few seconds. It can be noted that the pressure curves in Fig. 12 are not smooth but present a large number of oscillations. Once again, as brought out in the Section 4.2, here we consider local (within a narrow band) and instantaneous values of particle pressure. The timescale of the records, relatively small compared to the smoothing time scale, explains the rather noisy signal observed in Fig. 12.

Several simulations were carried out with different obstacle heights ranging from 1 to 5 cm, showing that the peak pressure value increases with this height. It is particularly interesting to compare the computed peak pressure value in the presence of an obstacle with pressures that can be deduced from the reference flow. With this goal in mind, here, we consider two possible reference pressures:

- the peak pressure value of the reference flow (as mentioned previously, it is close to the hydrostatic pressure under the maximum flow depth). This peak pressure $P_{\mathrm{ref}}^{10\%} = 2200\,\mathrm{Pa}$ on a 10% slope and $P_{\mathrm{ref}}^{20\%} = 1800\,\mathrm{Pa}$ on a 20% slope.
- the theoretical dynamic pressure of the reference flow, defined as $P_{\mathrm{th}} = \rho\overline{U}^2$ with ρ the density and $\overline{U}$ the mean velocity over the reference flow cross-section (over the flow depth in the 2D case presented here). This theoretical dynamic pressure $P_{\mathrm{th}}^{10\%} = 1090\,\mathrm{Pa}$ on a 10% slope and $P_{\mathrm{th}}^{20\%} = 1970\,\mathrm{Pa}$ on a 20% slope.

Table 2 Peak pressure applied to the obstacle compared to both reference pressures

Reference pressure	Maximum pressure of reference flow P_{ref}		Theoretical dynamic pressure $P_{\mathrm{th}}=\rho U^2$	
Slope	10%	20%	10%	20%
H_{obs}=1 cm	1.14	1.39	2.29	1.27
H_{obs}=2 cm	1.82	1.94	3.67	1.77
H_{obs}=3 cm	2.5	3.05	5.04	2.79
H_{obs}=4 cm	3.18	3.61	6.42	3.3
H_{obs}=5 cm	3.86	3.89	7.8	3.55

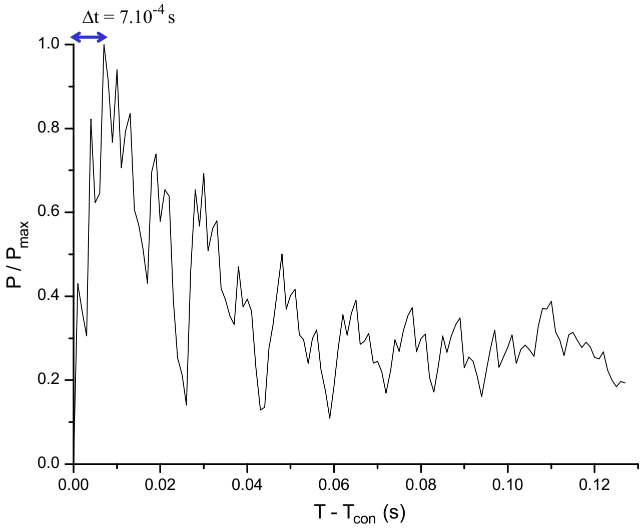

Fig. 13 Evolution of pressure versus time with obstacle height H_{obs}= 5 cm and slope=20%, detailed part showing the time of the pressure increase between the first contact and the pressure peak: 7.10^{-4} s in this case

The comparison of the simulated peak pressure value in presence of an obstacle to both reference pressures is presented in Table 2. As can be seen in this table, the peak pressure in the presence of an obstacle is systematically higher than the peak pressure of the reference flow. The ratio between these pressures shows moderate values for the lowest height of obstacle considered, H_{obs}=1 cm, but increases regularly with this value up to values of approximately 4 for the height of the obstacle H_{obs}=5 cm. Similar conclusions can be drawn when considering the theoretical dynamic pressure as the reference pressure. In that case, however, the ratio between the peak pressure in presence of an obstacle and the reference pressure can reach values of approximately 8 in the case of H_{obs}=5 cm with slope=10%. In practice, protection structures against mudflows or debris flows are often designed by considering the hydrostatic or the dynamic pressure and multiplying this value by an empirical safety coefficient. The results presented here show that actual peak pressures depend a great deal on flow conditions and reach values roughly five to ten times the theoretical dynamic pressure. This ratio is higher than the safety coefficients classically used by field engineers, which typically range from 2 to 5.

4.3.2 The pressure rising phase

To investigate precisely the rising phase of stresses applied to the obstacle, we conducted one simulation with a high frequency of data storage. For this simulation, presented in Fig. 13, we stored results every 10^{-4} s with the obstacle height H_{obs}=5 cm and the slope=20%. The timescale begins at the moment of first contact T_{con} of the particles with the obstacle, and the pressure is scaled by the peak pressure value P_{max}=6,990 Pa. It can be noted that the pressure jumps very quickly from 0 to the peak pressure within a period of time of 7.10^{-4} s. Only two oscillations, whose intensity is limited, precede the peak value. After the peak, the pressure immediately drops, showing no constant phase, so that residual pressure is only 1/4 of the peak pressure only 0.1 s later. For the same reasons as for the case illustrated in Fig. 12 (see Section 4.3.1), Fig. 13 shows large oscillations in the simulated pressure, whose amplitude clearly diminishes with time. The period of these oscillations varies with the density smoothing time step adopted, thus, proving the major influence of this parameter. However, varying the smoothing time step does not modify the peak pressure value. In addition, three different values of the numerical sound speed (c=20, 35, and 150 m s^{-1}) were adopted to carry out the same simulation. Within this range of variation, the sound speed value influences neither the peak pressure nor the duration of its rising phase.

5 Conclusion and perspectives

Understanding and quantifying mudflow–structure interactions and debris flow–structure interactions is of paramount importance for the rational design of technical countermeasures against these phenomena, but can also be used for the assessment of potential damage to human infrastructures. However, to date, only a limited number of studies have been conducted on this subject. We have presented here a numerical approach to this topic using a new numerical model based on the SPH method. After presenting the main features of the numerical model, we showed how well it simulates experimental, unsteady free-surface flows of viscoplastic fluids in the absence of an obstacle. On the basis of this first very positive result, we conducted a prospective study based only on numerical simulations, which analyzed the effect of simple obstacles perpendicular to the main flow direction. Two main topics were investigated: first, we studied the flow downstream of the obstacle to compute the momentum reduction attributable to the presence of an obstacle; second, we studied the pressure in the vicinity of the upstream face of the obstacle to compute the stresses applied on this obstacle, their peak intensity, and evolution over time. It must be noted that the present study is based on the computation of local and instantaneous variables at a scale which, given the inevitably limited number of particles, is at the limit of SPH capacities. The results presented are valuable but remain theoretical and still need to be confirmed. In other words, the numerical model has to be seen as a tool whose goal is to help us in analyzing impact features but which still needs to be validated by further numerical investigations, and of course, by comparison to experiments. Such experiments are currently in progress at Cemagref. In these experiments, we produce a rapid release of a transparent viscoplastic fluid (mixture of water and Carbopol®). Internal properties of the flows in the vicinity of obstacles (immediately upstream or at a distance downstream of the obstacle) are measured using the Particle Image Velocimetry technique and stress sensors installed on the upstream face of the obstacle measure the pressure and its evolution over time. However, the experimental study of the interaction phenomenon is not sufficient for several reasons: first, it is always difficult to respect similarity criteria; consequently, results established on a small scale cannot all be transposed to the real scale. Second, measurement techniques have their own limitations so that, for example, it is not currently possible to install a large number of pressure sensors on the obstacle. Alternatively, the numerical investigation does not have this type of limitation, but confidence in the models can only be obtained when they have been sufficiently compared to experiments. Consequently, one can reasonably assume that neither the numerical nor the experimental investigation is sufficient in itself to fully characterize the impact phenomenon. This is why we have adopted a general strategy of studying mudflow–structure interactions and debris flow–structure interactions combining experiments and numerical models. The present paper has essentially presented the latter tool within the whole approach.

Acknowledegements This study was supported by the European Union under the 5th Framework Programme: contract THARMIT EVG1-CT-1999-00012

References

1. Armanini, A., Scotton, P.: Experimental analysis on the dynamic impact of a debris flow on structures. Proceedings of the international symposium Interpreavent 1992, Bern Switzerland, **6**, 107–116 (1992)
2. Chen, C.L.: Generalized viscoplastic modeling of debris flow. J. Hydraul. Eng. ASCE **114**(3), 237–258 (1988)
3. Coussot, P.: Steady laminar flow of concentrated mud suspensions in open channel. J. Hydraul. Res. **32**(4), 535–559 (1994)
4. Coussot, P.: Mudflow Rheology and Dynamics. IAHR monograph, Balkema, Rotterdam (1997)
5. Denlinger, R.P., Iverson, R.M.: Flow of variably fluidized granular masses across three-dimensional terrain. 2. Numerical predictions and experimental tests. J. Geophys. Res. **106**(B1), 553–566 (2001)
6. Denlinger, R.P., Iverson, R.M.: Granular avalanches across irregular three-dimensional terrain: 1. Theory and computation. J. Geophys. Res. **109**, F01014 (2004)
7. Gray, J.M.N.T., Tai, Y.-C., Noelle, S.: Shock waves, dead zones and particle-free regions in rapid granular free-surface flows. J. Fluid Mech. **491**, 161–181 (2003)
8. Huebl, J., Fiebiger, G.: Debris-flow mitigation measures. In: Jakob, M., Hungr, O. (eds.) Debris-flow Hazards and Related Phenomena, pp. 445–487. Spinger-Praxis books in geophysical sciences, Springer-Verlag, Berlin Heidelberg, New York (2005)
9. Iverson, R.M., Denlinger, R.P.: Flow of variably fluidized granular masses across three-dimensional terrain. 1. Coulomb mixture theory. J. Geophys. Res. **106**(B1), 537–552 (2001)
10. Iverson, R.M., Logan, M., Denlinger, R.P.: Granular avalanches across irregular three-dimensional terrain: 2. Experimental tests. J. Geophys. Res. **109**, F01015 (2004)
11. Johnson, A.M.: Physical processes in geology. W. H. Freeman, San Francisco, Calif. (1970)
12. Jop, P., Forterre, Y., Pouliquen, O.: A constitutive law for dense granular flows. Nature **441**, 727–730 (2006)
13. Lachamp, P., Naaim, M., Faug, T., Laigle, D.: Simulation of the effect of defense structures on granular flows, using SPH. Natural Hazards and Earth System Sciences **2**, 203–209 (2002)
14. Lachamp, P.: Modélisation numérique de l'effet d'un obstacle sur les écoulements de fluides à seuil par la méthode SPH. PhD thesis, Université Joseph Fourier, Grenoble, France (2003) (in French)
15. Laigle, D., Coussot, P.: Numerical modelling of mudflows. J. Hydraul. Eng. **123**(7), 617–623 (1997)
16. Lucy, L.B.: A numerical approach to the testing of the fission hypothesis. Astron. J. **82**(12), 1013–1024 (1977)
17. Monaghan, J.J., Gingold, R.A.: Shock simulations by the particle method SPH. J. Comput. Phys. **52**, 374–389 (1983)
18. Monaghan, J.J.: An introduction to SPH. Comput. Phys. Comm. **48**, 89–96 (1988)
19. Monaghan, J.J.: On the problem of penetration in particle methods. J. Comput. Phys. **82**, 1–15 (1989)
20. Monaghan, J.J.: Simulating free surface flow using SPH. J. Comput. Phys. **110**, 399–406 (1994)
21. Patra, A.K., Bauer, A.C, Nichita, C.C., Pitman, E.B., Sheridan, M.F., Bursik, M., Rupp, B., Webber, A., Stinton, A.J., Namikawa, L.M., Renschler, C.S.: Parallel adaptative numerical simulation of dry avalanches over natural terrain. J. Volcanol. Geotherm. Res. **139**, 1–21 (2005)
22. Piau, J.-M.: Flow of a yield stress fluid in a long domain. Application to flow on an inclined plane. J. Rheol. **40**(4), 711–724 (1996)
23. Pierson, T.C.: Hyperconcentrated flow – transitional process between water flow and debris flow. In: Jakob, M., Hungr, O. (eds.) Debris-flow Hazards and Related Phenomena, pp. 159–202. Spinger-Praxis books in geophysical sciences, Springer-Verlag, Berlin, Heidelberg, New York (2005)
24. Rickenmann, D., Laigle, D., McArdell, B.W., Hübl, J.: Comparison of 2D debris-flow simulation models with field events. Comput. Geosci. **10**, 241–264 (2006)
25. Rodriguez-Paz, M.X., Bonet, J.: A corrected smooth particle hydrodynamics method for the simulation of debris flows. Numer. Methods Partial Differ. Equ. **20**, 140–163 (2004)
26. Zanuttigh, B., Lamberti, A.: Experimental analysis of the impact of dry avalanches on structures and consequences for debris-flows. J. Hydraul. Res. **44**(4), 522–534 (2006)